International Journal for Numerical and Analytical Methods in Geomechanics

WILEY

RESEARCH ARTICLE OPEN ACCESS

Insights Into the Mechanisms Controlling the Residual Strength of Bio-cemented Sands

Aoxi Zhang[1,2] | Frédéric Collin[2] | Antoine Wautier[3] | Anne-Catherine Dieudonné[1]

[1]Department of Geoscience & Engineering, Delft University of Technology, Delft, the Netherlands | [2]Urban and Environmental Engineering Research Unit, University of Liège, Liège, Belgium | [3]INRAE, Aix Marseille University, Marseille, France

Correspondence: Anne-Catherine Dieudonné (a.a.m.dieudonne@tudelft.nl)

Received: 24 June 2025 | **Revised:** 29 December 2025 | **Accepted:** 6 January 2026

Keywords: biocementation | DEM | residual strength | strain localisation

ABSTRACT

Microbially induced carbonate precipitation (MICP) is an emerging technique for enhancing the mechanical properties of granular soils. Although several experimental studies have reported increased shear strength in MICP-treated soils at both peak and residual states, other findings have shown reductions in residual strength compared to untreated soils. This study uses the discrete element method (DEM) to investigate the mechanisms governing the residual strength of bio-cemented sands. The results indicate that residual strength may decrease when carbonate precipitates in the form of grain-bridging patterns. In that case, the introduction of carbonates alters the contact network and may induce metastable configurations, particularly when the bonds are weak or non-cohesive. These configurations are prone to strain localisation upon shearing, leading to the development of shear bands and a reduction in residual strength. Conversely, higher cohesive strength enhances microstructural stability, offsetting the weakening effects of localisation. The residual strength of bio-cemented sands is therefore governed by two competing mechanisms, namely bond-induced stabilisation and instability-driven localisation.

1 | Introduction

Microbially induced carbonate precipitation (MICP) and enzyme induced carbonate precipitation (EICP) are promising methods for enhancing the mechanical performance of soils. Both processes promote the precipitation of calcium carbonate ($CaCO_3$) within the soil pore space, where it can act as a cementing agent that binds soil grains together. As a result, soils treated with MICP or EICP typically exhibit increased stiffness and strength [1–8], highlighting the potential of these methods for improving soil mechanical behaviour.

Experimental studies showed that bio-cementation can affect the mechanical behaviour of the treated soil, with the strength improvement being highly dependent on the carbonate content [5, 9–11]. Specifically, the bio-cemented sample with a relatively low carbonate content shows a slight improvement in peak and residual strengths compared to the uncemented sample. As the carbonate content increases, both the peak and residual strengths of the bio-cemented sample increase. Of particular interest to this study is the residual strength. In general, the residual strength of bio-cemented samples is higher than that of the uncemented sample [5, 12, 13]. This observation aligns with the intuitive expectation that bio-cementation should enhance soil strength at all deformation stages, including the residual state, even if the improvement is modest or negligible. However, some studies have shown that bio-cemented soils can exhibit a lower strength than uncemented soils at the residual state. Such reduction in residual strength has not been observed in classical cemented soils or rocks. This counterintuitive phenomenon has been observed, yet remains unexplained, in reported experiments on bio-cemented soils [13–18]. The relevant data is summarised in Figure 1.

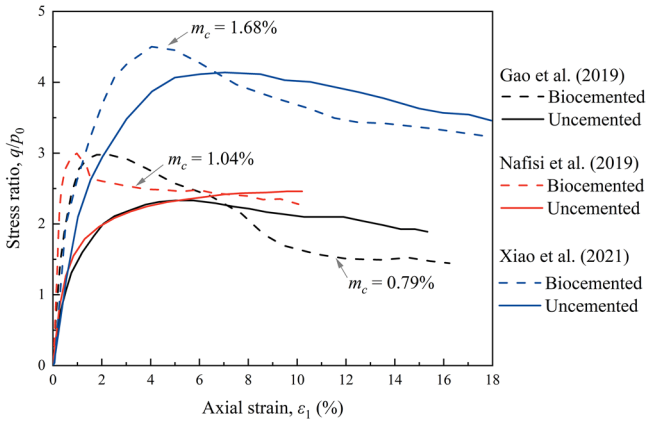

FIGURE 1 | Experimental evidence illustrates cases where the residual strength of bio-cemented soil is lower than that of uncemented soil. The presented data from Gao et al. [15] and Nafisi et al. [17] were obtained from drained triaxial compression tests under 100 kPa of confinement, and the data from Xiao et al. [13] was tested in drained condition with 20 kPa of confinement. The initial void ratio is 0.612, 0.752 and 0.796 for Gao et al., Nafisi et al., and Xiao et al., respectively. The stress ratio is defined here as the deviatoric stress divided by the confining pressure. m_c is the carbonate content by mass.

Understanding the residual strength of bio-cemented soils is of critical engineering importance, particularly for assessing their mechanical behaviour at large deformations. In slope stability problems, for instance, the state of stress and strain is generally non-uniform along the potential failure surface; some zones may have reached and softened beyond peak strength, while others are still mobilising it. This spatial variation in mobilised strength is central to understanding progressive failure mechanisms and ensuring realistic stability assessments in bio-cemented slopes.

The discrete element method (DEM) has been widely used to reveal the underlying mechanism of soil behaviour benefiting from its full access to microscopic quantities [19–21]. The decrease in residual strength exhibited by bio-cemented soil was not captured in DEM models for (bio-)cemented soils [22–25]. This can be attributed to the fact that the effects of cementation are usually simulated by introducing virtual bonds between soil grains instead of explicitly modelling cement agents [24, 26–29]. In this way, the cementing material (i.e., bond in DEM) is assumed to be located at sand grain contacts. Such a simplification leads to the residual strength of cemented samples equivalent to or above that of the uncemented sample and is not able to capture the post-breakage behaviour since the virtual bonds disappear after breakage. Moreover, the role of cementing material located elsewhere in the pore space of the soil is ignored. Recently, a 3D DEM study by Zhang and Dieudonné [30] reported that the bio-cemented DEM specimen with a specific microstructure can exhibit a lower residual strength than the uncemented DEM specimen. In that study, DEM was used to explicitly model both sand and carbonate particles, with a focus on the role of carbonate distribution pattern (i.e., the location of carbonate particles with respect to the sand grains). Four typical carbonate distribution patterns were modelled, namely grain bridging, contact cementing, grain coating and pore filling. It was found in Zhang and Dieudonné [30] that carbonates distributed in the pattern of bridging (i.e., connecting grains that were initially not in contact) led to a reduction in the residual strength of bio-cemented soil compared to that of uncemented soil, while other distribution patterns did not lead to a reduction in the residual strength. However, no mechanistic explanation was provided on such a phenomenon. Following Zhang and Dieudonné [30], this paper aims to elucidate the micro-origin of the residual strength reduction for the bridging type of cementation, seeking to understand not only why but also under what conditions this phenomenon happens.

This paper is organised as follows. Section 2 introduces the contact law and DEM model setup used in this study. In Section 3, a parametric study is carried out on 2D DEM samples. The samples are subjected to drained biaxial compression tests. The effect of carbonate content, sand-carbonate cohesive strength and their relative elastic modulus on the macroscopic mechanical behaviour of bio-cemented sands with the bridging type of cementation are systematically evaluated. It should be noted that 3D DEM results are also provided in Appendix A to further support the understanding of the mechanical behaviour of bio-cemented sands with the bridging type of cementation. In Section 4, a detailed discussion on the microscopic observation during the biaxial compression tests is provided to understand the underlying mechanism. Finally, major findings from this paper are summarised in Section 5.

2 | DEM Simulations

2.1 | Contact law

The discrete element simulations are performed using the open-source platform YADE [31]. A cohesive-frictional contact model, based on the classical linear elastic-plastic law from [32] and accounting for rolling and twisting resistance, is used.

For two spheres of radii R_1 and R_2 in contact, the normal force $\boldsymbol{F}_n$, incremental shear force $\Delta\boldsymbol{F}_s$, incremental rolling moment $\Delta\boldsymbol{M}_r$ and incremental twisting moment $\Delta\boldsymbol{M}_{tw}$ are calculated as:

$$\boldsymbol{F}_n = k_n u_n \boldsymbol{n} \tag{1}$$

$$\Delta\boldsymbol{F}_s = -k_s \Delta\boldsymbol{u}_s \tag{2}$$

$$\Delta\boldsymbol{M}_r = -k_r \Delta\theta_r \tag{3}$$

$$\Delta\boldsymbol{M}_{tw} = -k_{tw} \Delta\theta_{tw} \tag{4}$$

where u_n is the relative normal displacement of the two spheres, $\boldsymbol{n}$ is the normal contact vector, $\Delta\boldsymbol{u}_s$ is the incremental tangential displacement, and $\Delta\theta_r$ and $\Delta\theta_{tw}$ are the relative rotations due to rolling and twisting respectively. k_n, k_s, k_r and k_{tw} are the contact normal stiffness, tangential stiffness, rolling stiffness and twisting stiffness respectively, which are given by:

$$k_n = \frac{2E_1R_1E_2R_2}{E_1R_1 + E_2R_2} \tag{5}$$

$$k_s = \nu k_n \tag{6}$$

$$k_r = \alpha_r R_1 R_2 k_s \tag{7}$$

$$k_{tw} = \alpha_{tw} R_1 R_2 k_s \tag{8}$$

where E_i $(i = 1, 2)$ is the modulus of elasticity of sphere i, ν is the stiffness ratio, and α_r and α_{tw} are the rolling and twisting stiffness coefficients respectively.

The normal, shear, rolling and twisting resistances are equal to:

$$F_n^{max} = \sigma_{coh} \min(R_1, R_2)^2 \tag{9}$$

$$F_s^{max} = ||\boldsymbol{F}_n|| \tan \varphi_c' + \sigma_{coh} \min(R_1, R_2)^2 \tag{10}$$

$$M_r^{max} = ||\boldsymbol{F}_n|| \eta_r \min(R_1, R_2) \tag{11}$$

$$M_{tw}^{max} = ||\boldsymbol{F}_n|| \eta_{tw} \min(R_1, R_2) \tag{12}$$

where σ_{coh} is a cohesive strength parameter which controls the adhesion forces in the normal and tangential directions. In this study, cohesion is introduced only at sand-carbonate contacts (S-C); therefore, σ_{coh} specifically denotes σ_{coh}^{S-C}. φ_c' is the contact friction angle, and η_r and η_{tw} are the resistance coefficients of rolling and twisting, respectively.

2.2 | Sample preparation

In a 1 m × 2 m domain, 10,000 spherical particles are randomly generated with all the particle centres located in a single layer. Four rigid walls are used as the boundary condition, representing a simplification compared to the flexible membrane used in physical tests. The 2D condition is simulated by placing the centres of all spheres on the same plane and blocking the translation and rotations in the out-of-plane direction. The radius expansion method is adopted for isotropic compression, during which the radii of the particles increase until the sample reaches a target confining pressure p_0 (kPa). After that, the radius expansion is then turned off to fix the size of the particles. The radii of sand grains are uniformly distributed with an average diameter (d_{50}) of 13.62 mm and a size ratio (d_{max}/d_{min}) of 2. Then the inter-particle friction angle is adjusted to reach a target void ratio of 0.225. Note that the void ratio in 2D is defined as the area of voids to the area of solids in the plane in which the centres of particles lie. In the meantime, the rigid walls are controlled by a servomechanism to maintain the confining pressure. After the generation of the host sand sample with target void ratio and confining pressure, $CaCO_3$ particles are introduced into the host sand sample [33]. All the $CaCO_3$ particles are deployed at sand grain gaps to form the bridging type of distribution as demonstrated in Figure 2. It should be noted that the SEM image presented in Figure 2a is used solely to establish the physical basis for the bridging cementation concept modelled in our DEM simulations.

The DEM samples are subjected to drained biaxial compression tests. The sand particle parameters are calibrated so that the stress-strain response of the uncemented DEM specimen closely matches the experimental results reported by Nafisi et al. [5], as compared in Figure 3. Following that, the Young's modulus of carbonate particle is set to be 0.9 times that of sand particles [35]. The sand-carbonate cohesion (σ_{coh}^{S-C}) is adjusted for the bridging sample with $m_c = 2.2\%$ to ensure its peak deviatoric stress ratio matches that observed in the cemented specimen with equivalent m_c from Nafisi et al. [5]. The remaining contact parameters of carbonate particles, including φ_c', α_r, α_{tw}, η_r, η_{tw}, are assumed to be the same as those of the sand particles [30] due to the lack of experimental data. Overall, the DEM model reproduces the magnitudes of the peak and residual strength of the experimental results, and captures the key mechanical effects of cementation, including increased stiffness and enhanced dilatancy compared to the uncemented specimen. The adopted DEM parameters are summarised in Table 1.

3 | Macroscopic Response

In this section, 2D DEM samples are subjected to drained biaxial compression tests. A parametric study is carried out to investigate the effect of carbonate content (m_c), sand-carbonate cohesion (σ_{coh}^{S-C}), carbonate/sand stiffness ratio (E_c/E_s) and confining pressure (p_0) on the mechanical response, specifically the residual strength of the bridging type of cemented samples. The four parameters considered in the parametric study are listed in Table 2. It should be noted that this study derives insights from 2D DEM simulations because it is easy to visualise quantities or features, such as strain localisation (if any) and microstructure evolution in two dimensions [20, 21, 36, 37]. However, results from equivalent 3D DEM simulations are provided in Appendix A and used to support the understanding of the macroscopic mechanical behaviour.

3.1 | Effect of Carbonate Content

Figure 4 shows the stress–strain response and volumetric behaviour of samples with different carbonate contents from drained biaxial compression tests under 100 kPa of confinement. $E_c/E_s = 0.9$ and $\sigma_{coh}^{S-C} = 200$ MPa in the bridging samples presented in Figure 4. It can be seen that for all the carbonate contents under consideration, all the cases show a reduction in residual strength compared to the uncemented sample. This suggests that the increase in carbonate content in the considered range does not eliminate this phenomenon. The same finding holds with the 3D DEM simulation presented in Figure A1a,b.

To validate the DEM model, the results for the sample with $m_c = 1\%$ and 2.2% are further compared against laboratory test from Gao et al. [15], as shown in Figure 5. The experimental cemented sample with $m_c = 0.79\%$ exhibits a characteristic behaviour: it achieves a higher peak strength compared to the uncemented sample (dashed black line), but its residual strength at large strains is lower than that of the uncemented sample. The DEM simulations at different carbonate contents successfully reproduce this qualitative behaviour. Both DEM cemented samples show enhanced peak strength but reduced residual strength compared to the DEM uncemented sample.

3.2 | Effect of Sand-Carbonate Cohesion

Figure 6 shows the effect of sand-carbonate cohesion (σ_{coh}^{S-C}) on the stress-strain and volumetric behaviour of bridging type of

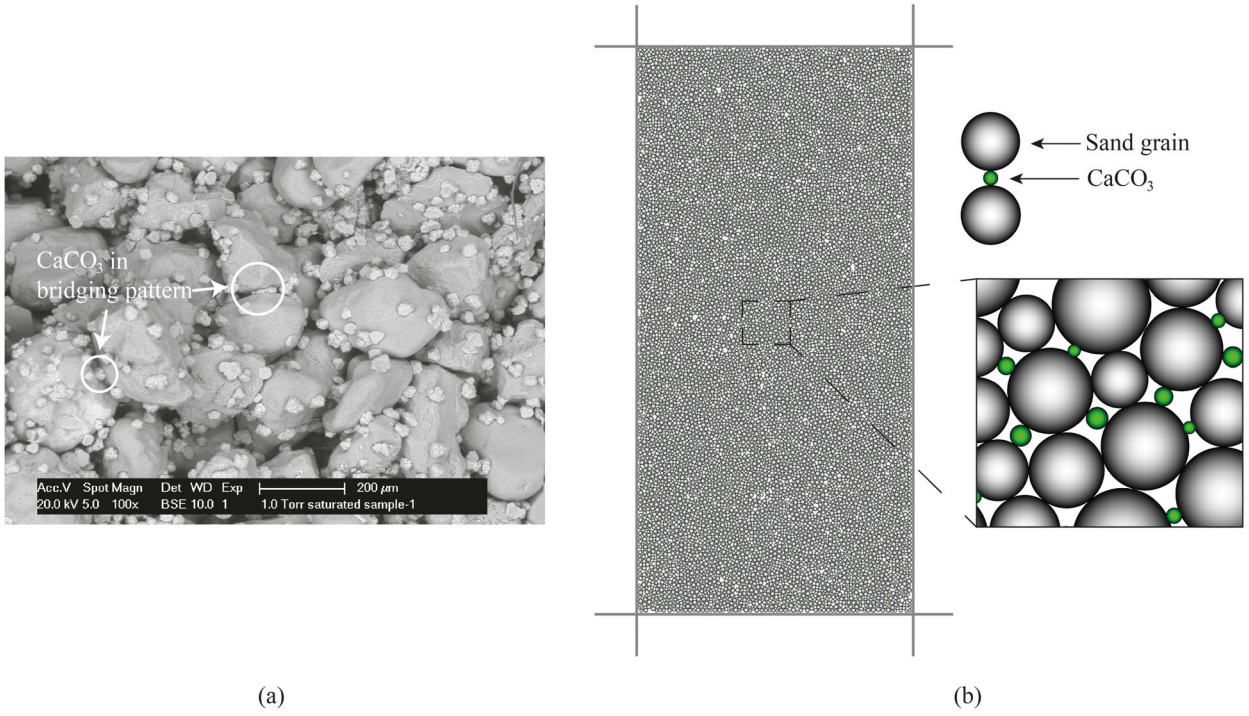

FIGURE 2 | (a) Microscopic observation on bio-cemented sands showing grain-bridging cementation, the SEM image is from van Paassen [34]; (b) Illustration of a 2D DEM cemented sample with the bridging type of cementation.

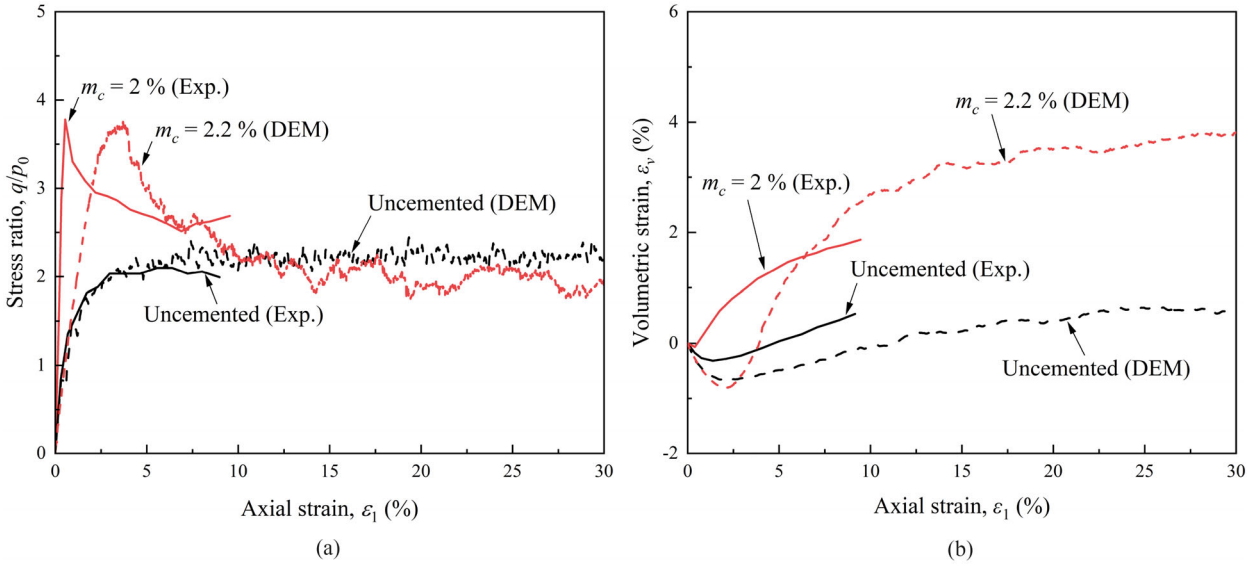

FIGURE 3 | Comparison of DEM simulations and experimental results from Nafisi et al. [5]: (a) stress-strain behaviours; (b) volumetric responses. $E_c/E_s = 0.9$ and $\sigma_{coh}^{S-C} = 200$ MPa for the cemented DEM specimen with $m_c = 2.2\%$ in this plot. All tests are conducted under 100 kPa of confining pressure.

samples tested under 100 kPa of confinement. $E_c/E_s = 0.9$ and $m_c = 2.2\%$ in the bridging samples presented in Figure 6. It can be seen that σ_{coh}^{S-C} plays a crucial role in the residual strength of cemented samples. The residual strength of the bridging sample with a low σ_{coh}^{S-C} is lower than that of the uncemented sample. With the increasing of σ_{coh}^{S-C}, the residual strength of the bridging type of sample increases to the same level as the uncemented sample and finally exceeds the uncemented sample. It should be noted that a case with $\sigma_{coh}^{S-C} = 0$ MPa is also included in Figure 6. In this case, the carbonate particles are non-cohesive. The case with $\sigma_{coh}^{S-C} = 0$ MPa also shows a reduction in the residual strength compared to the uncemented sample, indicating that the bridging pattern is one of the key factors that lead to such behaviour. In terms of volumetric behaviour, those bridging samples that exhibit a lower residual strength than the uncemented sample show a lower enhancement in dilatancy. As σ_{coh}^{S-C} increases, the sample tends to dilate more. The 3D DEM results presented in Figure A1c,d confirm the same finding as observed in Figure 6.

TABLE 1 | Properties of particles used in the 2D DEM simulations.

Properties	Symbol	Unit	Sand/ Carbonate
Density	ρ	kg/m^3	2650 / 2710
Elastic modulus	E	MPa	200 / 180
Stiffness ratio	ν	—	0.3 / 0.3
Friction angle	φ_c'	°	16 / 16
Rolling stiffness coefficient	α_r	—	0.4 / 0.4
Twisting stiffness coefficient	α_{tw}	—	0.4 /0.4
Rolling resistance coefficient	η_r	—	0.4 / 0.4
Twisting resistance coefficient	η_{tw}	—	0.4 / 0.4

TABLE 2 | Summary of parametric variations.

Varying parameter	Varying range	Fixed parameter and value
m_c (%)	1; 2.2; 3.5	$E_c/E_s = 0.9$, $p_0 = 100$ kPa, $\sigma_{coh}^{S-C} = 200$ MPa
σ_{coh}^{S-C} (MPa)	0; 100; 200; 800	$E_c/E_s = 0.9$, $p_0 = 100$ kPa, $m_c = 2.2\%$
E_c/E_s (-)	0.1; 0.2; 0.9	$p_0 = 100$ kPa, $\sigma_{coh}^{S-C} = 200$ MPa, $m_c = 2.2\%$
p_0 (kPa)	50; 100; 200	$E_c/E_s = 0.9$, $\sigma_{coh}^{S-C} = 200$ MPa, $m_c = 2.2\%$

3.3 | Effect of Sand-Carbonate Stiffness Ratio

The motivation for testing various stiffness ratios of carbonate with respect to sand (E_c/E_s) is that different materials can precipitate in MICP treatment, including vaterite, aragonite, calcite and other metastable hydrated forms [38–41]. A detailed review can be found in Zhang et al. [35]. These precipitations exhibit different elastic moduli, ranging from 25 GPa to 91.28 GPa, which leads to E_c/E_s varying from 0.3 to 1.2, given that elastic modulus of quartz sand is around 77 GPa. Figure 7 shows the effect of the ratio of E_c/E_s on the stress-strain and volumetric behaviour of bridging type of samples, with $m_c = 2.2\%$ and $\sigma_{coh}^{S-C} =$ 200 MPa tested under 100 kPa of confinement. It can be found that the ratio of E_c/E_s affects the residual strength of the bridging type of sample with respect to the uncemented sample. Specifically, a lower E_c/E_s leads to a minor difference in the residual strength between the bridging type of sample and the uncemented sample. When E_c approaches E_s, e.g., at $E_c = E_s$, the bridging type of sample shows a reduction in the residual strength. The observed trend agrees with the 3D DEM results presented in Figure A1e,f.

In the case of calcite as the precipitation, which is observed in most MICP experiments, E_c/E_s is around 0.9, lying in the range which exhibits lower residual strength than the uncemented sample. This again suggests that it is possible for bridging type of bio-cemented soils to exhibit a lower residual strength than uncemented soil.

3.4 | Effect of Confining Pressure

Figure 8 shows the effect of confining pressure on the stress–strain behaviour of bridging type of samples (with $m_c = 2.2\%$, $\sigma_{coh}^{S-C} = 200$ MPa and $E_c/E_s = 0.9$). It can be seen that the bridging sample exhibits a lower residual strength than the uncemented sample across all confining pressures examined. This agrees with the experimental observations, as shown in Figure 1, in which such a phenomenon is observed from triaxial compression tests under different confining pressures. However, while this phenomenon persists at all confinement levels, the reduction in residual strength becomes less pronounced with increasing confining pressure. The observed trend can be further supported by the 3D DEM results presented in Figure A1g,h, which show a consistent trend as the 2D results presented in Figure 8.

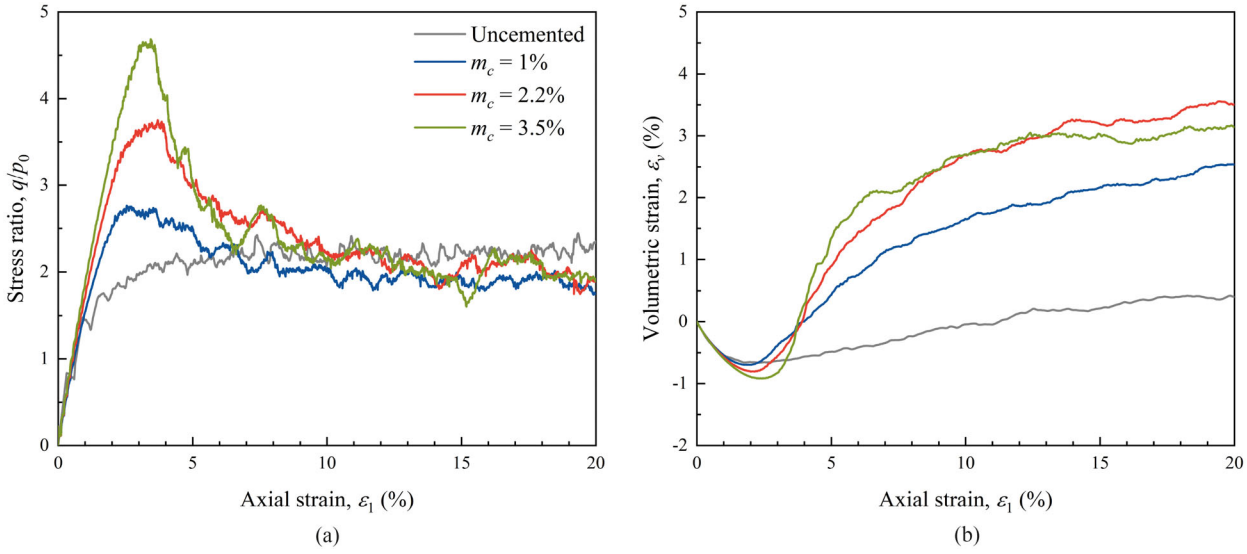

FIGURE 4 | (a) Stress-strain and (b) volumetric behaviour of bridging samples with different carbonate contents (m_c).

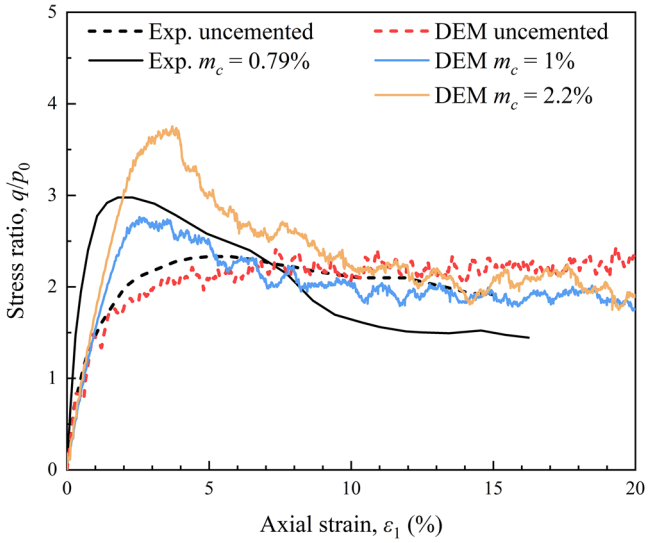

FIGURE 5 | Comparison of stress-strain behaviours of DEM results against laboratory tests from Gao et al. [15]. All tests are conducted under 100 kPa of confining pressure.

4 | Microscopic Observations

The 2D and 3D DEM results indicate that the overall mechanical behaviour of cemented samples depends on the relative elastic modulus of carbonate and sand (E_c/E_s) and the sand-carbonate cohesive strength (σ_{coh}^{S-C}). Yet, the mechanisms by which these variables affect the mechanical response – particularly the residual strength – remain unclear. To gain deeper insight into this, microscopic insights derived from 2D DEM simulations are explored in this section.

4.1 | Kinematic Fields

As observed in Section 3, the introduction of carbonate particles in the form of bridging increases the brittleness of the samples, which may be understood from the kinematic fields [42–44]. Therefore, the kinematic pattern of uncemented sample and bridging type of samples with different σ_{coh}^{S-C} and E_c/E_s are analysed and compared as follows.

The kinematic field of the 2D uncemented sample, 2D bridging type of sample with p_0 = 100 kPa, m_c = 2.2%, E_c/E_s = 0.9 and σ_{coh}^{S-C} = 0 MPa, 100 MPa, 200 MPa and 800 MPa are compared in Figure 9. The kinematic field is described by the incremental deviatoric strain field. The increment is from the state of 1% axial strain prior to the state of interest to the interested state. The detailed calculation of the incremental strain fields can refer to [45]. The effect of σ_{coh}^{S-C} can be investigated by comparing the cases with different σ_{coh}^{S-C}. Five interesting states marked in the stress-strain curve of each case are selected to demonstrate the evolution of the kinematic field, covering pre-peak state, peak state, post-peak state and residual state.

In general, a diffuse mode can be identified from the contours of the incremental deviatoric strain field for the uncemented sample shown in Figure 9a. In contrast, as cohesionless particles introduced (Figure 9b), strain localisation develops at the beginning of the post-peak phase. This indicates that the introduction of cohesionless particles in the bridging pattern can result in the development of strain localisation.

The localisation pattern of the bridging type of sample with σ_{coh}^{S-C} = 100 MPa is similar to the case of σ_{coh}^{S-C} = 0 as shown in Figure 9. A well-developed shear band can be observed at the post-peak state (state 3) in the case of σ_{coh}^{S-C} = 100 MPa. Comparing the bridging type of sample with σ_{coh}^{S-C} = 0 and σ_{coh}^{S-C} = 100 MPa, it can be seen that the presence of cohesion σ_{coh}^{S-C} changes the kinematic pattern in the post-peak phase. As σ_{coh}^{S-C} increases to 200 MPa and 800 MPa, the development of shear band becomes less significant.

Overall, the introduction of carbonate particles in the bridging pattern, whether they are cohesive or not, modifies the kinetic pattern of the sample and leads to the formation of shear bands. This finding is consistent with the experimental observation

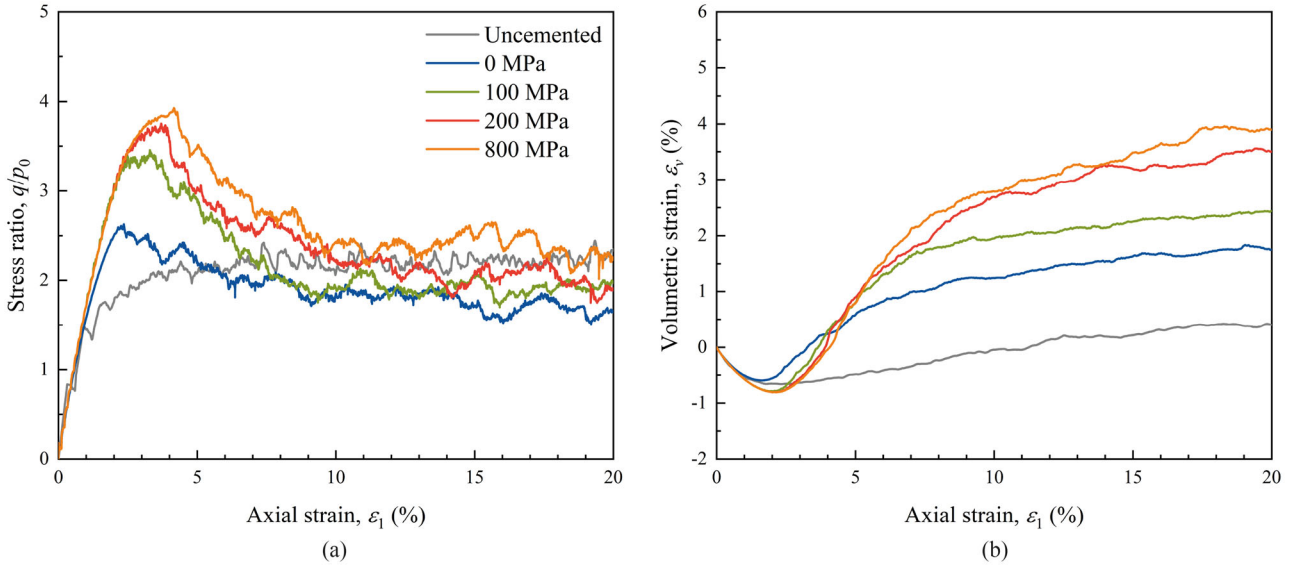

FIGURE 6 | (a) Stress-strain and (b) volumetric behaviour of bridging type of samples with different sand-carbonate cohesion (σ_{coh}^{S-C}).

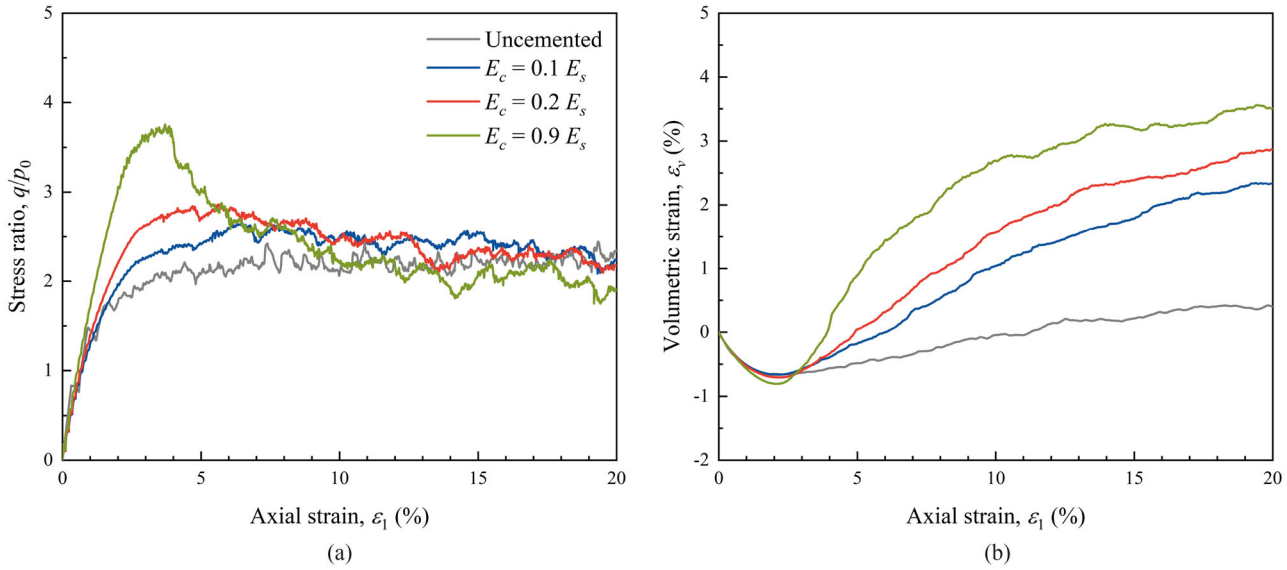

FIGURE 7 | (a) Stress-strain and (b) volumetric behaviour of 2D bridging samples with different ratios of E_c/E_s.

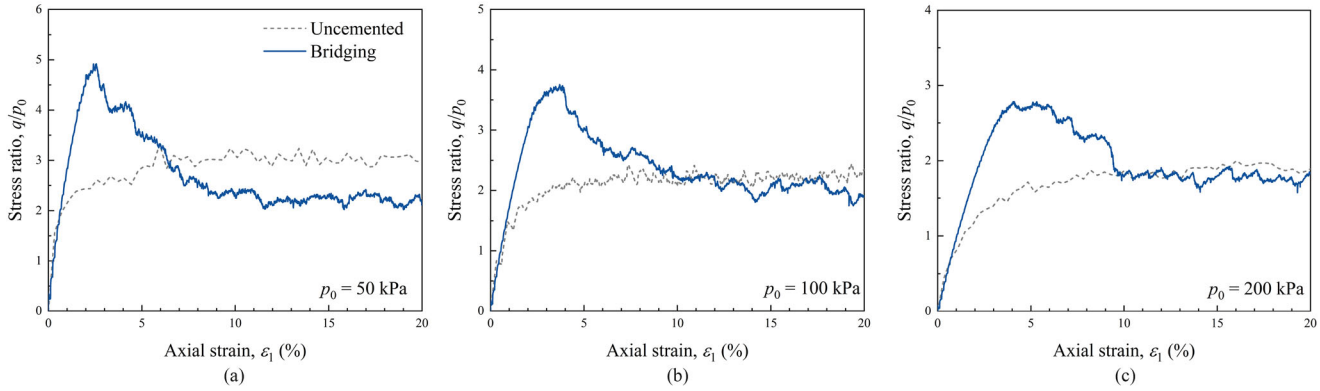

FIGURE 8 | Stress–strain behaviour of bridging samples at different confining pressures.

reported by [13], in which repetitive mechanical tests were carried out on MICP-treated sands and it was found that those treated samples showing lower residual stress tend to exhibit apparent shear bands. Comparing the cases of $\sigma_{coh}^{S-C} = 100$ MPa, 200 MPa and 800 MPa, it can be seen that a shear band is more clearly developed at the beginning of the post-peak state (state 3) for the case with a lower σ_{coh}^{S-C}. In addition, the formed shear band shows a more pronounced development for the case with a lower σ_{coh}^{S-C}. This suggests that the bridging samples with a lower σ_{coh}^{S-C} suffer from a more severe strain localisation and hence more stress reduction. These findings support that the residual strength of the bridging type of sample shows a decreasing trend with the decrease of σ_{coh}^{S-C}. The difference in the development of strain localisation can be explained by the difference in the bond breakage behaviour and the microstructure evolution, which are discussed in the following sections.

It is worth noting that the bridging type of sample with a high σ_{coh}^{S-C} (e.g., 800 MPa case) shows strain localisation but exhibits higher residual strength than that of the uncemented sample. This is because, on the one hand, for the bridging type of samples with various σ_{coh}^{S-C}, the formation of the shear band(s) in the post-peak phase weakens the sample, leading to the possibility of a lower residual strength than the uncemented sample. On the other hand, cohesive carbonates are introduced in the sample, and not all the bonds are broken in the post-peak phase (details are presented in Section 4.2). The unbroken bonds can contribute to the increase of the residual strength of the sample, resulting in the possibility of a higher residual strength than the uncemented sample. Consequently, both mechanisms, namely, the formation of shear bands, which weakens the sample, and the left cohesive bonds, which enhance the sample, compete with each other and, together, dominate the overall residual strength. When σ_{coh}^{S-C} is low, the weakening effect due to the formation of the shear band is dominant. With the increasing of σ_{coh}^{S-C}, the contribution to residual strength manifests, which leads to an increasing trend of residual strength with σ_{coh}^{S-C}. For a high σ_{coh}^{S-C}, the contribution from the remaining bonds exceeds the weakening effect, resulting in a higher residual strength than that of the uncemented sample.

Figure 10 presents the kinematic pattern of bridging type of sample with $m_c = 2.2\%$, $E_c/E_s = 0.1$ and $\sigma_{coh}^{S-C} = 200$ MPa. The effect of E_c/E_s can be assessed by comparing this case with the

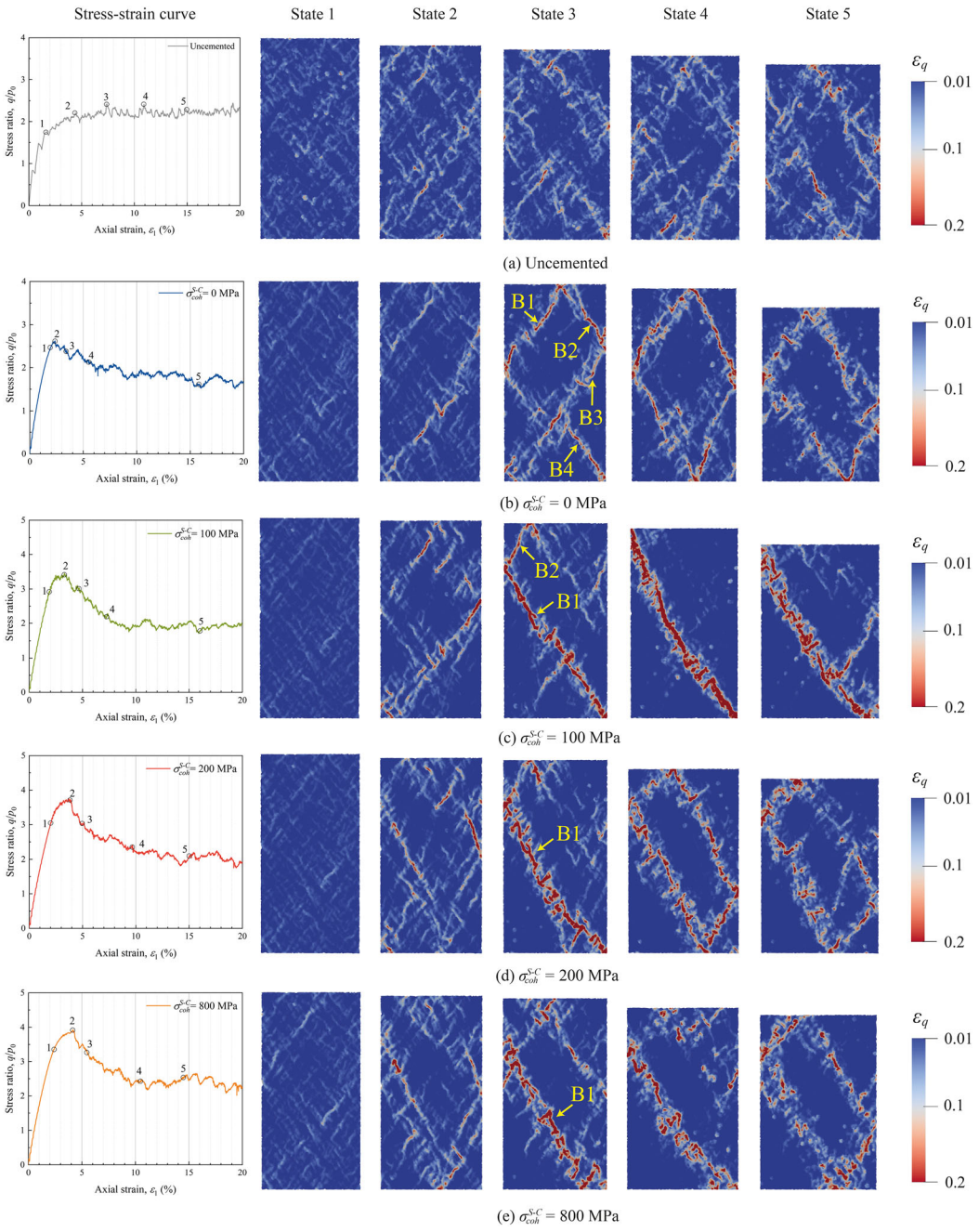

FIGURE 9 | Effect of cementation and sand-carbonate cohesive strength (σ_{coh}^{S-C}) on the evolution of the incremental deviatoric strain field. E_c/E_s = 0.9 is used for simulations presented herein.

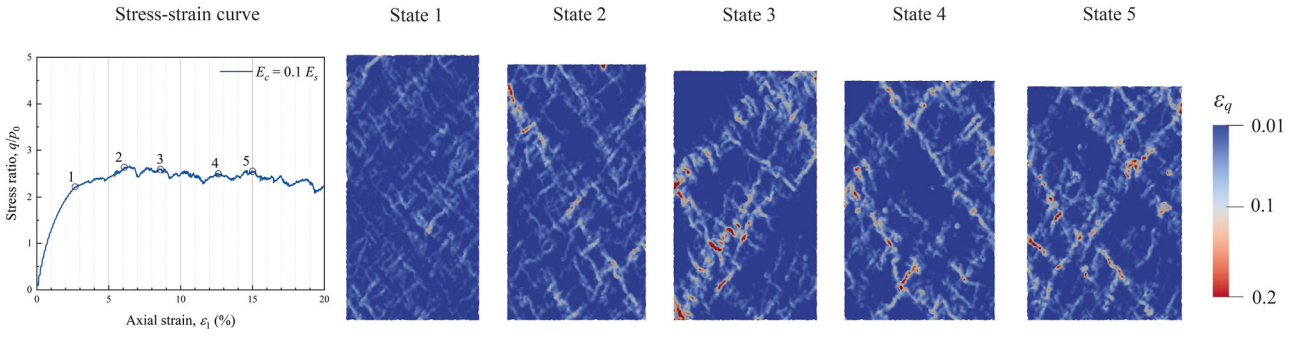

FIGURE 10 | Incremental deviatoric strain contour of bridging type of sample with σ_{coh}^{S-C} = 200 MPa, E_c/E_s = 0.1.

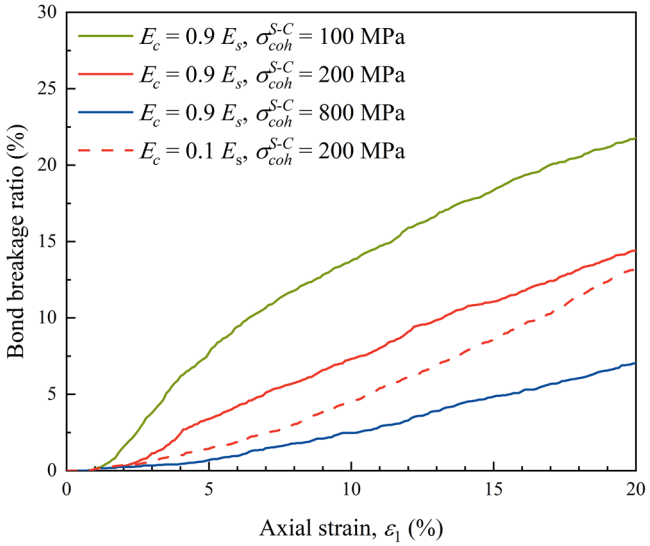

FIGURE 11 | Evolution of bond breakage ratio of the bridging type of samples with various σ_{coh}^{S-C}.

bridging sample of $E_c/E_s = 0.9$, $\sigma_{coh}^{S-C} = 200$ MPa (see Figure 9d). It can be seen from Figure 10 that there is no mature shear band developed during the shearing and it can be characterised as diffuse deformation. This kinematic pattern is similar to the uncemented sample, which also shows a diffuse pattern. By contrast, it is obviously different from the bridging sample with $E_c/E_s = 0.9$ and $\sigma_{coh}^{S-C} = 200$ MPa in which clear shear bands are identified. This suggests that the bridging sample with a higher E_c/E_s suffers from more severe strain localisation during the post-peak phase and thus exhibits a lower residual strength than the one with a lower E_c/E_s.

4.2 | Bond Breakage Behaviour

The evolution of bond breakage ratio of the bridging type of samples with different magnitudes of σ_{coh}^{S-C} is compared in Figure 11 (solid lines). where $m_c = 2.2\%$ and $p_0 = 100$ kPa for all cases. The bond breakage ratio is defined as the ratio of the number of broken $CaCO_3$ bonds to the number of initial $CaCO_3$ bonds. A similar evolution trend of bond breakage ratio can be observed in all three cases, in which the bond breakage ratio increases with the progress of shearing. In addition, a higher σ_{coh}^{S-C} leads to a lower bond breakage ratio, suggesting that more bonds are reserved for the case with a higher σ_{coh}^{S-C}. The spatial distribution of breakage events, correlating with the incremental deviatoric strain field at the selected five states, is presented in Figure 12. Cases of $\sigma_{coh}^{S-C} =$ 100 MPa and 800 MPa are compared in Figure 12. It can be seen that for the case of $\sigma_{coh}^{S-C} = 100$ MPa, breakage events (red dots) occur in most areas of the specimen. Those areas which suffer from strain localisation show intensive breakage. This is more obvious in the case of $\sigma_{coh}^{S-C} = 800$ MPa, in which the areas where breakage events occur are highly consistent with areas where strain localisation is present. These findings support that not all the bonds are broken in the post-peak phase and more bonds are retained with a higher σ_{coh}^{S-C}.

The evolution of the bond breakage ratio of bridging type of samples with different E_c/E_s is also compared in Figure 11 (red colour). It can be seen that the bridging sample with $E_c/E_s = 0.9$

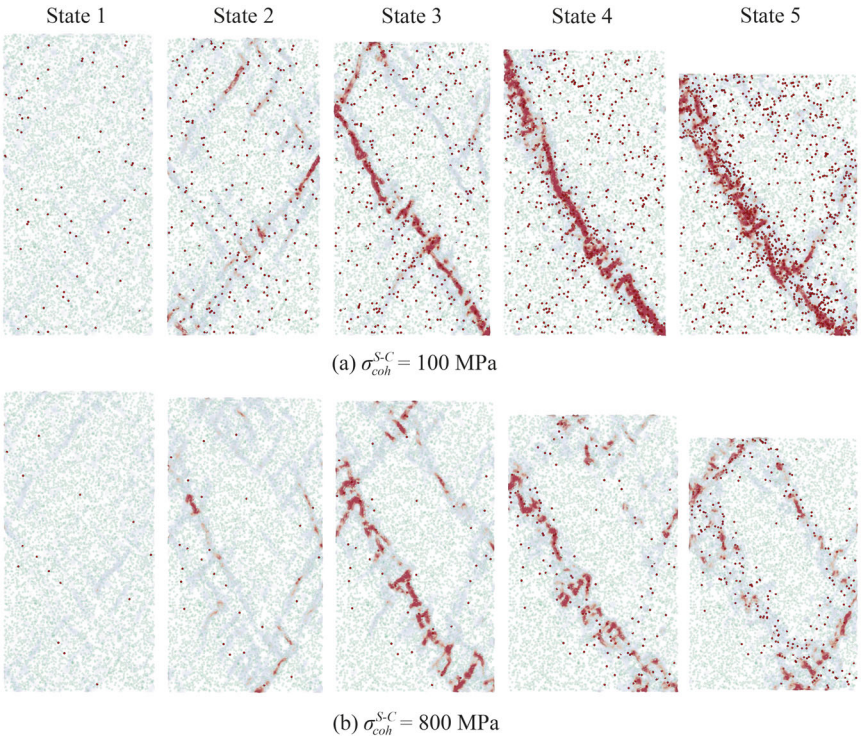

FIGURE 12 | Spatial distribution of breakage events correlating with the incremental deviatoric strain field. Cases of $p_0 = 100$ kPa, $m_c = 2.2\%$ and $E_c/E_s = 0.9$: (a) $\sigma_{coh}^{S-C} = 100$ MPa and (b) $\sigma_{coh}^{S-C} = 800$ MPa. Red dots represent the broken $CaCO_3$ bonds, and translucent green ones for unbroken $CaCO_3$ bonds. Note that the sizes of the dots are identical for better visualisation.

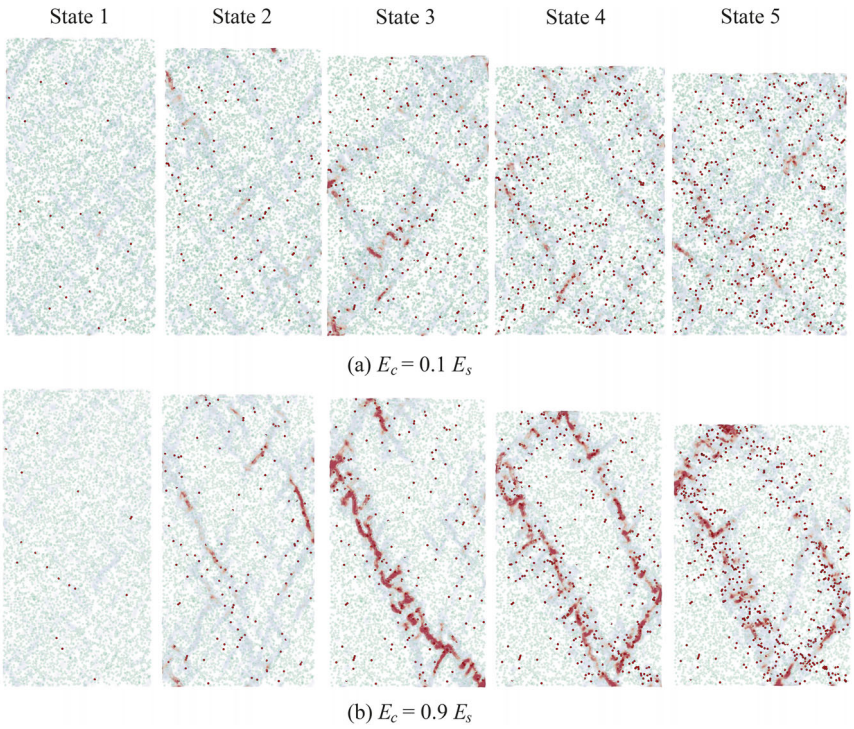

FIGURE 13 | Spatial distribution of breakage events correlating with the incremental deviatoric strain field. Cases of $p_0 = 100$ kPa, $m_c = 2.2\%$ and $\sigma_{coh}^{S-C} = 200$ MPa: (a) $E_c/E_s = 0.1$ and (b) $E_c/E_s = 0.9$. Red dots represent the broken $CaCO_3$ bonds and translucent green ones for unbroken $CaCO_3$ bonds. Note that the sizes of the dots are identical for better visualisation.

shows a slightly higher bond breakage ratio than the one with $E_c/E_s = 0.1$. However, the spatial distribution of breakage events of the two cases is quite different, as presented in Figure 13. The breakage events are dispersed throughout the bridging sample with $E_c/E_s = 0.1$, corresponding to a diffuse deformation pattern. By contrast, the distribution of breakage events of the case with $E_c/E_s = 0.9$ is more concentrated, aligning with the distribution of strain localisation.

4.3 | Grain-Scale Instability and Microstructure Evolution

In Section 4.1, it is found that the introduction of carbonate particles in the bridging pattern modifies the kinetic pattern of the sample and leads to the formation of shear bands. In this section, how the introduction of carbonate particles in the bridging pattern initiates the formation of the shear band is discussed from the grain scale.

It is well-accepted that the formation of a shear band is due to the relative movement of particles. Indeed, the introduction of non-cohesive or low-cohesive carbonates in the bridging pattern may affect the stability of the mesostructure, and hence relative movement is more likely to occur at a sand-carbonate contact than a sand-sand contact. To compare the stability of a sand-sand contact and a sand-carbonate contact, an analytical test of grain sliding is carried out on the two types of contacts respectively, as demonstrated in Figure 14. The grain-sliding test aims at examining the tolerance of deflection causing relative sliding, in which the grain below (either sand or carbonate) is fixed and the upper sand grain is free of translation (note that only translation is considered here, rolling is discussed later). A constant vertical force F is applied on the upper sand grain. The deflection d is characterised by the horizontal distance between the centres of the upper sand and the grain below. Note that a vertical displace-

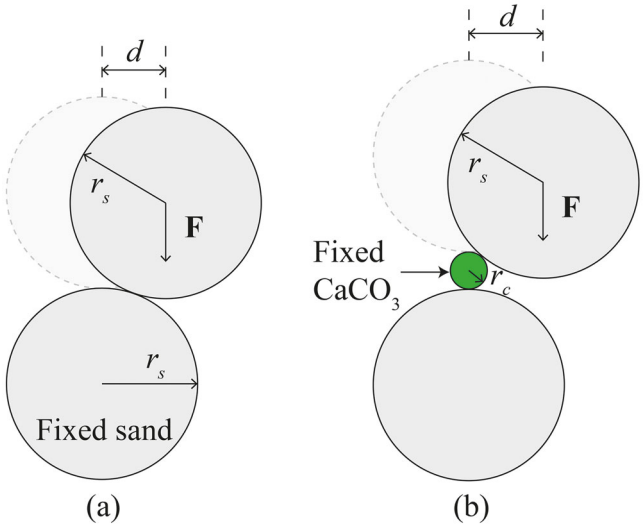

FIGURE 14 | Demonstration of two-particle assembly stability test for (a) sand-sand contact and (b) sand-carbonate contact. The radius of the upper sand and bottom sand (r_s) is the same as the average radius of all sand particles in the 2D DEM sample, $r_s = 6.81$ mm. The radius of the carbonate particle r_c is equal to the average radius of all carbonate particles in the 2D DEM sample, $r_c = 1.24$ mm. Consequently, $r_c/r_s = 0.182$, which is in line with the typical size ratio of carbonate to sand particle [46].

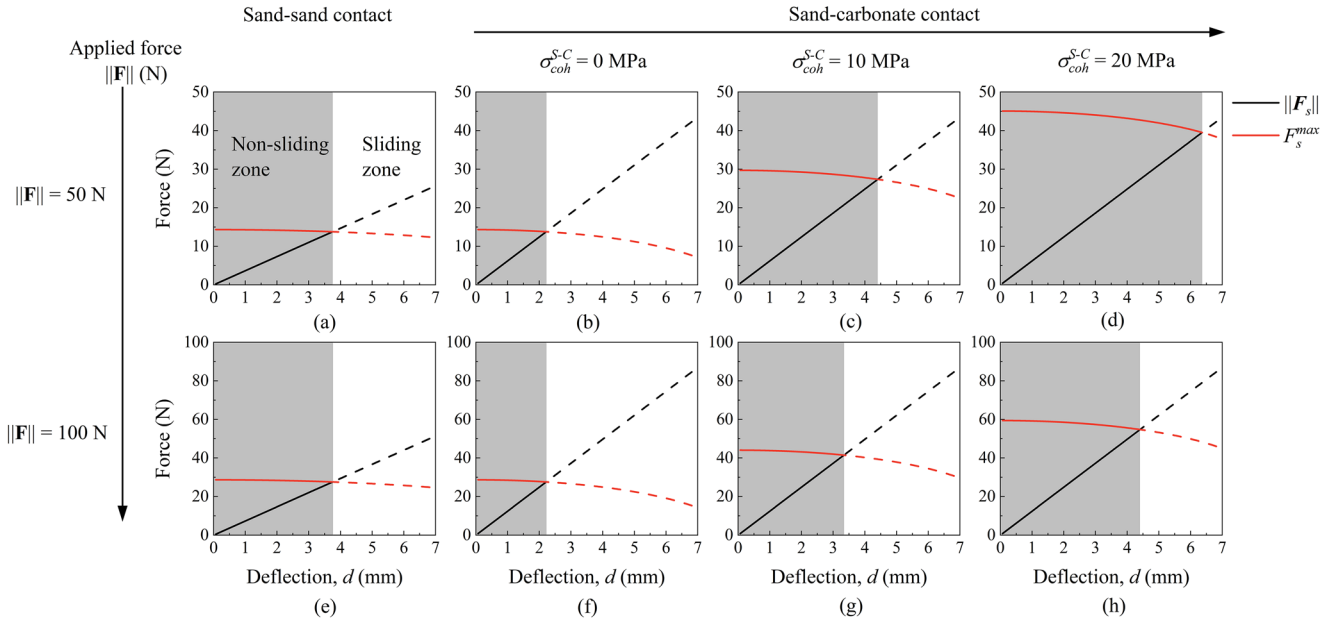

FIGURE 15 | Comparison of critical deflection triggering sliding for sand-sand contact and sand-carbonate contact with various σ_{coh}^{S-C}.

ment is introduced correspondingly upon the applied deflection so that the two grains remain in contact. In the case that the upper sand is vertically placed with respect to the bottom grain, namely, $d = 0$ (position represented by dash circle in Figure 14), no sliding will occur in the two contacts. With the increase of d, there is a possibility that sliding occurs, depending on whether the shear force $||\boldsymbol{F}_s||$ reaches the maximum shear force F_s^{max}. The larger the critical d that just triggers sliding, the more stable the two-grain assembly.

Figure 15 presents the results of grain-sliding tests. In each test scenario, the evolution of shear force $||\boldsymbol{F}_s||$ and the maximum shear force F_s^{max} with the deflection d are plotted. In the grey area where $||\boldsymbol{F}_s|| < F_s^{max}$, there is no sliding and hence characterised as the non-sliding zone. For those where $||\boldsymbol{F}_s|| > F_s^{max}$, sliding occurs. Figure 15a–d show the results for cases of sand-sand contact and sand-carbonate contact with various σ_{coh}^{S-C} under 50 N of vertical force applied on the upper sand grain. Figure 15e,f presents the results for cases under 100 N of applied vertical force. By comparing Figure 15a,b or e,f, it can be seen that at a given applied force, a larger d is needed to trigger sliding for sand-sand contact, while the non-cohesive sand-carbonate contact can only tolerate a smaller deflection before sliding. In addition, with the increase of σ_{coh}^{S-C}, the non-sliding zone of the sand-carbonate contact increases and can exceed the critical deflection of the sand-sand contact. These findings indicate that a sand-sand contact is able to withstand greater disturbance without sliding, while the introduction of non-cohesive carbonate, or carbonate with low cohesion, tends to form a metastable structure which is more prone to sliding. Moreover, a higher σ_{coh}^{S-C} can compensate for this instability and lead to a more stable structure.

It should also be noted that by comparing Figure 15c and g or d and h, given the same σ_{coh}^{S-C}, the sand-carbonate contact exhibit a larger non-sliding zone at a lower applied force. This finding supports that a bridging sample with a low E_c/E_s tends to be more stable at grain scale than one with a higher E_c/E_s, since the average sand-carbonate contact force in the former case is lower than that of the later case (see Figure 16).

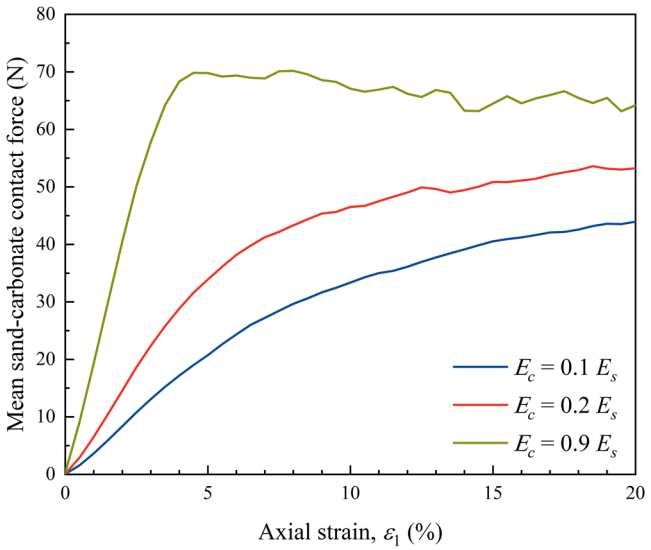

FIGURE 16 | Evolution of mean sand-carbonate contact force for bridging type of cemented samples with various E_c/E_s. $p_0 = 100$ kPa, $m_c = 2.2\%$ and $\sigma_{coh}^{S-C} = 200$ MPa in the bridging samples presented herein.

Apart from grain sliding, relative rolling between the two particles in contact can also occur. Taking the same cases as demonstrated in Figure 14, in which the bottom grain (either sand or carbonate) is fixed and the upper sand grain is free of rolling. As the applied force F goes through the centre of the upper grain, a moment is generated, which may drive relative rolling of the upper grain with respect to the bottom particle, depending on whether the rolling moment $||\boldsymbol{M}_r||$ reaches the maximum rolling moment M_r^{max}. The larger the critical d that just triggers rolling, the more

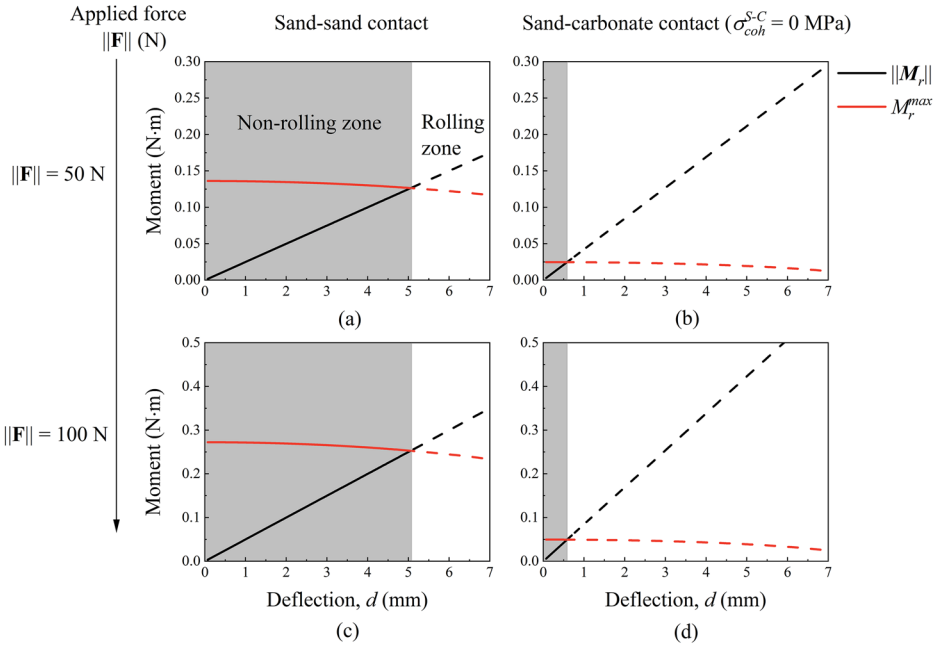

FIGURE 17 | Comparison of critical deflection triggering rolling for sand-sand contact and sand-carbonate contact.

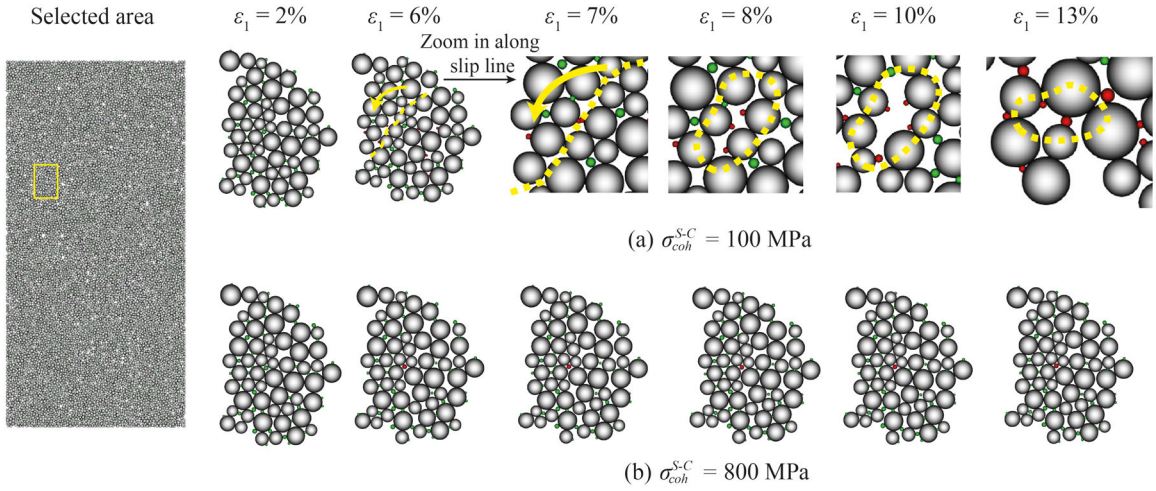

FIGURE 18 | Microstructure evolution of the bridging type of samples (p_0 = 100 kPa, m_c = 2.2% and E_c/E_s = 0.9): (a) σ_{coh}^{S-C} = 100 MPa, (b) σ_{coh}^{S-C} = 800 MPa. The grey particle represents sand grain, the green one represents the unbroken carbonate bond, and the red one represents the broken carbonate bond.

stable the two-grain assembly against rolling. Figure 17 presents the results of grain-rolling tests. It should be noted that cohesion is not introduced in the rolling direction (see Section 2.1), hence the response of sand-carbonate contact with various σ_{coh}^{S-C} is the same as the case of $\sigma_{coh}^{S-C} = 0$. It can be seen from Figure 17 that sand-carbonate contact exhibits significantly less non-rolling area than sand-sand contact, indicating the instability of sand-carbonate contacts against rolling. This finding suggests that rolling is more prone to occur at sand-carbonate contacts.

The difference in grain-scale stability further affects the arrangement of particles at the meso-scale (the scale considering a group of particles). To elaborate on how σ_{coh}^{S-C} affects the particle arrangement at the mesoscale, a group of particles is monitored to demonstrate their evolution upon shearing. Figure 18 compares the micro-architecture evolution of the selected particles of cemented samples with σ_{coh}^{S-C} = 100 MPa and 800 MPa. It can be seen that, for σ_{coh}^{S-C} = 100 MPa, the arrangement of the particles remains the same until reaching an axial strain of 6%, while bond breakage occurs until then. The broken bonds create areas prone to slippage, as indicated by the dash lines in Figure 18a. From 6% to 7% of axial strain, the left portion of the particles moves along the slip lines (indicated by the dashed yellow line) relative to the right portion. From 7% to 10% axial strain, the left portion continues to move, creating a large local void. In contrast, the right portion shows no obvious relative movement. As shearing proceeds to 13% axial strain, more bonds break, and the left portion undergoes subsequent rearrangement, leading to

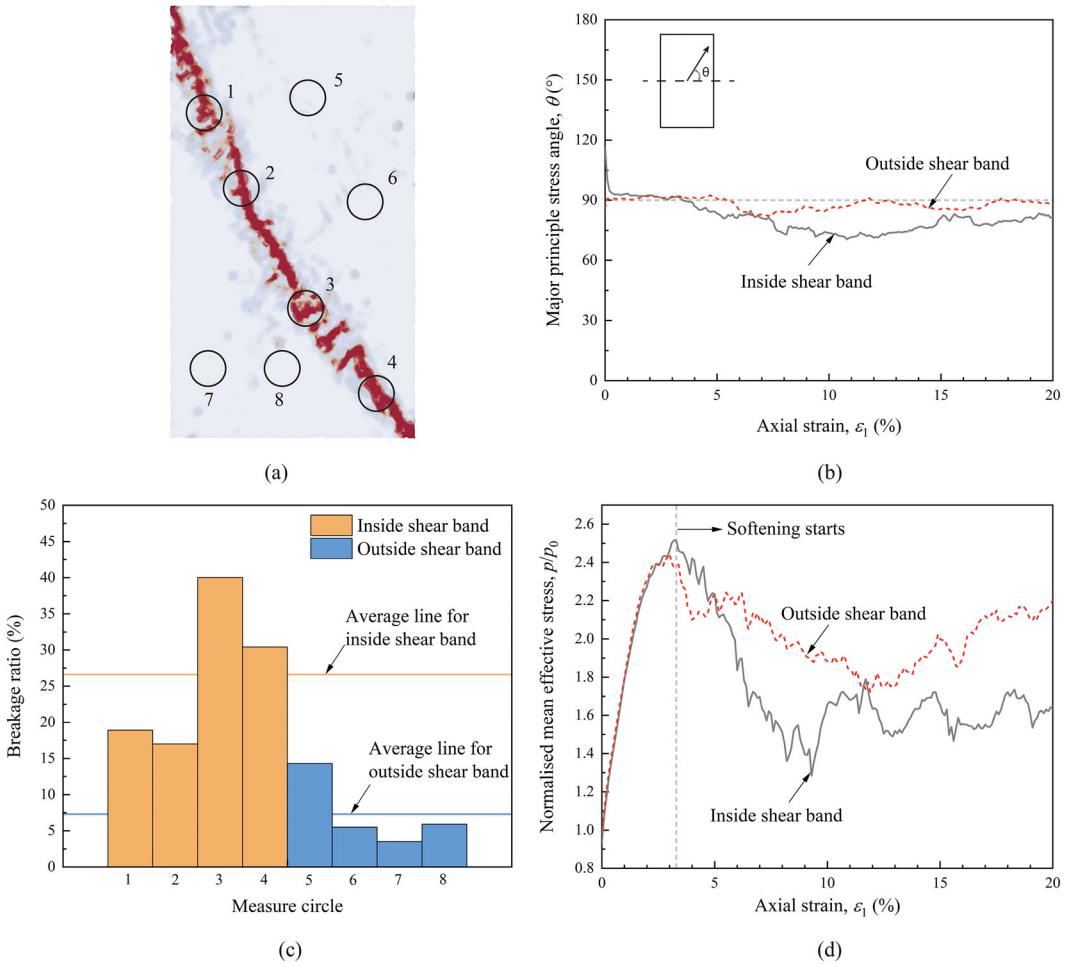

FIGURE 19 | (a) Illustration of the eight selected measure circles; (b) Evolution of major principle stress angle with axial strain; (c) Bond breakage ratio in each measure circle at state 4 (refer to Figure 9c); (d) Evolution of normalised mean effective stress with axial strain. Data from the bridging sample with σ_{coh}^{S-C}=100 MPa and $E_c = 0.9E_s$.

the collapse of the void. On the other hand, for $\sigma_{coh}^{S-C} = 800$ MPa, it can be seen that fewer bonds break, and the microstructure remains almost the same during the whole process, as shown in Figure 18b. By comparing both cases, it can be inferred that σ_{coh}^{S-C} plays an important role in the particle rearrangement. A higher σ_{coh}^{S-C} can limit particle rearrangement and contribute to forming a more stable micro-architecture and therefore a higher strength.

4.4 | Microscopic Behaviour Inside and Outside the Shear Band

Previous sections demonstrate that the introduction of carbonate particles in the bridging pattern can lead to the formation of shear bands. In this section, the link between shear band and softening (i.e., macroscopic stress reduction) is discussed.

To quantitatively describe the stress state in the shear band, a total of eight circles, four along the shear band and four outside the shear band (for the purpose of comparison) as indicated in Figure 19a, are used to measure the local variables. Each measure circle has a diameter of 149.8 mm, which is 11 times d_{50}. This size of the measure circle is sufficiently large (10-12 times d_{50} as suggested by [47]) so that the calculated stress values are unaffected by the size of the measure circle. The equivalent stress tensor is calculated from all the contacts located in that circle using the Love–Weber formula:

$$\sigma_{ij} = \frac{1}{V} \sum_{N^c} f_i^c l_j^c \tag{13}$$

where σ_{ij} is the stress tensor, V is the volume or surface in 2D under consideration, N_c is the number of contacts, f^c is the contact force and l^c is the branch vector connecting the centroids of the two particles in contact. From the stress tensor, the local mean effective stress (p) and the major principle stress direction (θ) can be derived. Figure 19b shows that the major stress direction inside the shear band deviates from the vertical direction (i.e., the main loading direction), indicating a structural change within the sample. Such a stress rotation can lead to structural softening [48]. The bond breakage ratio inside the shear band is significantly higher than that outside the shear band (Figure 19c). Moreover, the mean effective stress inside the shear band zone is obviously lower than that outside the shear band since the initiation of softening (Figure 19d), suggesting that the formation of the shear band weakens the overall stress within the packing.

5 | Conclusions

Experimental studies have shown that bio-cemented soils, which are generally expected to exhibit improved strength, may display lower residual strength than uncemented soils. This counter-intuitive phenomenon has not been systematically investigated and remains poorly understood. The present study addresses this issue through a series of DEM simulations designed to explain not only why but also under what conditions this phenomenon happens.

The results demonstrate that bio-cemented sands can exhibit reduced residual strength when carbonate precipitation occurs in the form of grain bridging. This response is governed primarily by the cohesive strength and relative stiffness of the precipitation-grain contacts, while the carbonate content (within the studied range) and confining pressure have negligible influence. Grain-scale analyses show that the presence of carbonates in a bridging pattern modifies the contact structure and introduces metastable configurations, particularly when the bonds are weak or non-cohesive. These conditions promote strain localisation, leading to the formation of shear bands and a corresponding reduction in residual strength. In contrast, stronger cohesive bonds enhance the stability of the microstructure and inhibit localisation, resulting in improved residual strength. The residual behaviour of bio-cemented sands is therefore controlled by the competition between two mechanisms: bond-induced stabilisation and instability-driven strain localisation. At low cohesive strength, the weakening effect of localisation dominates. As cohesive strength increases, the stabilising contribution becomes more significant, leading to a progressive increase in residual strength.

Author Contributions

Aoxi Zhang: conceptualisation, methodology, analysis, writing – original draft. **Frédéric Collin**: analysis, writing – review and editing, funding acquisition. **Antoine Wautier**: analysis, writing – review and editing. **Anne-Catherine Dieudonné**: conceptualisation, analysis, supervision, writing – review and editing.

Acknowledgments

This work was supported by the China Scholarship Council (CSC) and SAGE-SAND (Soil ageing around offshore wind turbine foundations - from operational response to decommissioning) project, funded by the Energy Transition Fund (ETF) of Belgium. The support is gratefully acknowledged.

Conflicts of Interest

The authors declare no conflicts of interest.

Data Availability Statement

Data are available from the corresponding author upon reasonable request.

References

1. L. Cheng, R. Cord-Ruwisch, and M. A. Shahin, "Cementation of Sand Soil by Microbially Induced Calcite Precipitation at Various Degrees of Saturation," *Canadian Geotechnical Journal* 50, no. 1 (2013): 81–90.

2. T. Hoang, J. Alleman, B. Cetin, K. Ikuma, and S.-G. Choi, "Sand and Silty-Sand Soil Stabilization Using Bacterial Enzyme–Induced Calcite Precipitation (BEICP)," *Canadian Geotechnical Journal* 56, no. 6 (2018): 808–822.

3. D. Terzis and L. Laloui, "Cell-Free Soil Bio-Cementation With Strength, Dilatancy and Fabric Characterization," *Acta Geotechnica* 14, no. 3 (2019): 639–656.

4. H. Yasuhara, D. Neupane, K. Hayashi, and M. Okamura, "Experiments and Predictions of Physical Properties of Sand Cemented by Enzymatically-Induced Carbonate Precipitation," *Soils and Foundations* 52, no. 3 (2012): 539–549.

5. A. Nafisi, B. M. Montoya, and T. M. Evans, "Shear Strength Envelopes of Biocemented Sands With Varying Particle Size and Cementation Level," *Journal of Geotechnical and Geoenvironmental Engineering* 146, no. 3 (2020): 04020002.

6. V. Krishnan, H. Khodadadi Tirkolaei, K. Martin, N. Hamdan, L. A. Van Paassen, and E. Kavazanjian Jr, "Variability in the Unconfined Compressive Strength of EICP-Treated "Standard" Sand," *Journal of Geotechnical and Geoenvironmental Engineering* 147, no. 4 (2021): 06021001.

7. J. Shi, Y. Xiao, J. A. H. Carraro, H. Li, H. Liu, and J. Chu, "Anisotropic Small-Strain Stiffness of Lightly Biocemented Sand Considering Grain Morphology," *Géotechnique* (2023), 1–14.

8. J.-P. Wang, M.-C. Li, M. Qi, S. Ge, and A. Dadda, "Micro-Macro Investigation on Bio-Cemented Sand Under Different Grouting Saturation: An Effective Enhancement Method," *Geomechanics for Energy and the Environment* 37 (2024): 100530.

9. H. Lin, M. T. Suleiman, D. G. Brown, and E. Kavazanjian Jr, "Mechanical Behavior of Sands Treated by Microbially Induced Carbonate Precipitation," *Journal of Geotechnical and Geoenvironmental Engineering* 142, no. 2 (2016): 04015066.

10. Y. Xiao, Y. Wang, C. Desai, X. Jiang, and H. Liu, "Strength and Deformation Responses of Biocemented Sands Using A Temperature-Controlled Method," *International Journal of Geomechanics* 19, no. 11 (2019): 04019120.

11. S. Wu, B. Li, and J. Chu, "Stress-Dilatancy Behavior of Micp-Treated Sand," *International Journal of Geomechanics* 21, no. 3 (2021): 04020264.

12. H. Lin, M. T. Suleiman, D. G. Brown, and E. Kavazanjian Jr, "Mechanical Behavior of Sands Treated by Microbially Induced Carbonate Precipitation," *Journal of Geotechnical and Geoenvironmental Engineering* 142, no. 2 (2015): 04015066.

13. Y. Xiao, Y. Wang, S. Wang, T. M. Evans, et al., "Homogeneity and Mechanical Behaviors of Sands Improved by A Temperature-Controlled One-Phase MICP Method," *Acta Geotechnica* 16, no. 5 (2021): 1417–1427.

14. F. Tagliaferri, J. Waller, E. Andò, et al., "Observing Strain Localisation Processes In Bio-Cemented Sand Using X-Ray Imaging," *Granular Matter* 13 (2011): 247–250.

15. Y. Gao, L. Hang, J. He, and J. Chu, "Mechanical Behaviour of Biocemented Sands at Various Treatment Levels and Relative Densities," *Acta Geotechnica* 14, no. 3 (2019): 697–707.

16. D. Terzis and L. Laloui, "A Decade of Progress and Turning Points In The Understanding of Bio-Improved Soils: A Review," *Geomechanics for Energy and the Environment* 19 (2019): 100116.

17. A. Nafisi, S. Safavizadeh, and B. M. Montoya, "Influence of Microbe and Enzyme-Induced Treatments on Cemented Sand Shear Response," *Journal of Geotechnical and Geoenvironmental Engineering* 145, no. 9 (2019): 06019008.

18. M.-J. Cui, J.-J. Zheng, J. Chu, C.-C. Wu, and H.-J. Lai, "Bio-Mediated Calcium Carbonate Precipitation and Its Effect on The Shear Behaviour of Calcareous Sand," *Acta Geotechnica* 16 (2021): 1377–1389.

19. X. Huang, C. O'sullivan, K. Hanley, and C. Kwok, "Discrete-Element Method Analysis of The State Parameter," *Géotechnique* 64, no. 12 (2014): 954–965.

20. B. Dai, J. Yang, and X. Luo, "A Numerical Analysis of The Shear Behavior of Granular Soil With Fines," *Particuology* 21 (2015): 160–172.

21. N. Deng, A. Wautier, Y. Thiery, Z.-Y. Yin, P.-Y. Hicher, and F. Nicot, "on The Attraction Power of Critical State In Granular Materials," *Journal of the Mechanics and Physics of Solids* 149 (2021): 104300.

22. Y.-H. Wang and S.-C. Leung, "A Particulate-Scale Investigation of Cemented Sand Behavior," *Canadian Geotechnical Journal* 45, no. 1 (2008): 29–44.

23. M. Jiang, W. Zhang, Y. Sun, and S. Utili, "An Investigation on Loose Cemented Granular Materials Via DEM Analyses," *Granular Matter* 15, no. 1 (2013): 65–84.

24. Z. Shen, M. Jiang, and C. Thornton, "DEM Simulation of Bonded Granular Material. Part I: Contact Model and Application To Cemented Sand," *Computers and Geotechnics* 75 (2016): 192–209.

25. P. Yang, S. O'Donnell, N. Hamdan, E. Kavazanjian, and N. Neithalath, "3D DEM Simulations of Drained Triaxial Compression of Sand Strengthened Using Microbially Induced Carbonate Precipitation," *International Journal of Geomechanics* 17, no. 6 (2017): 04016143.

26. S. Utili and R. Nova, "DEM Analysis of Bonded Granular Geomaterials," *International Journal for Numerical and Analytical Methods in Geomechanics* 32, no. 17 (2008): 1997–2031.

27. K. Feng, B. Montoya, and T. Evans, "Discrete Element Method Simulations of Bio-Cemented Sands," *Computers and Geotechnics* 85 (2017): 139–150.

28. P. Yang, E. Kavazanjian, and N. Neithalath, "Particle-Scale Mechanisms In Undrained Triaxial Compression of Biocemented Sands: Insights From 3D DEM Simulations With Flexible Boundary," *International Journal of Geomechanics* 19, no. 4 (2019): 04019009.

29. P. Yang, E. Kavazanjian, and N. Neithalath, "DEM Simulations on The Influence of Carbonate Precipitation on Liquefaction Mitigation of Sand," *Computers and Geotechnics* 162 (2023): 105681.

30. A. Zhang and A.-C. Dieudonné, "Effects of Carbonate Distribution Pattern on The Mechanical Behaviour of Bio-Cemented Sands: A DEM Study," *Computers and Geotechnics* 154 (2023): 105152.

31. V. Šmilauer, *Yade Documentation 3rd ed*. The Yade Project, 2021, http://yade-dem.org/doc/.

32. P. A. Cundall and O. D. Strack, "A Discrete Numerical Model For Granular Assemblies," *Géotechnique* 29, no. 1 (1979): 47–65.

33. A. Zhang and A.-C. Dieudonné, "Cementor: A Toolbox To Generate Bio-Cemented Soils With Specific Microstructures," *Biogeotechnics* (2024), 100081.

34. L. A. van Paassen, "Biogrout, Ground Improvement by Microbial Induced Carbonate Precipitation," Ph.D. dissertation, Delft University of Technology, 2009.

35. A. Zhang, V. Magnanimo, H. Cheng, T. J. Heimovaara, and A.-C. Dieudonné, "DEM Investigation Into The Small-Strain Stiffness of Bio-Cemented Soils," *Acta Geotechnica* 19, no. 10 (2024): 6809–6823.

36. N. Deng, A. Wautier, A. Tordesillas, et al., "Lifespan Dynamics of Cluster Conformations In Stationary Regimes In Granular Materials," *Physical Review E* 105, no. 1 (2022): 014902.

37. J. Liu, A. Wautier, W. Zhou, F. Nicot, and F. Darve, "Incremental Shear Strain Chain: A Mesoscale Concept For Slip Lines In 2D Granular Materials," *Granular Matter* 24, no. 4 (2022): 119.

38. M. Tlili, M. B. Amor, C. Gabrielli, S. Joiret, G. Maurin, and P. Rousseau, "Characterization of Caco3 Hydrates by Micro-Raman Spectroscopy," *Journal of Raman spectroscopy* 33, no. 1 (2002): 10–16.

39. Z. Zou, W. J. Habraken, G. Matveeva, et al., "A hydrated crystalline calcium carbonate phase: Calcium carbonate hemihydrate," *Science* 363, no. 6425 (2019): 396–400.

40. A. Clarà Saracho, S. K. Haigh, T. Hata, et al., "Characterisation of $CaCO_3$ Phases During Strain-Specific Ureolytic Precipitation," *Scientific Reports* 10, no. 1 (2020): 1–12.

41. A. C. Saracho, L. Lucherini, M. Hirsch, et al., "Controlling the Calcium Carbonate Microstructure of Engineered Living Building Materials," *Journal of Materials Chemistry A* 9, no. 43 (2021): 24 438–24 451.

42. N. Guo and J. Zhao, "3D Multiscale Modeling of Strain Localization In Granular Media," *Computers and Geotechnics* 80 (2016): 360–372.

43. H. Wu, N. Guo, and J. Zhao, "Multiscale Modeling and Analysis of Compaction Bands In High-Porosity Sandstones," *Acta Geotechnica* 13 (2018): 575–599.

44. H. Wu, W. Wu, W. Liang, F. Dai, H. Liu, and Y. Xiao, "3D DEM Modeling of Biocemented Sand With Fines as Cementing Agents," *International Journal for Numerical and Analytical Methods in Geomechanics* 47, no. 2 (2023): 212–240.

45. E. Catalano, B. Chareyre, and E. Barthélemy, "Pore-Scale Modeling of Fluid-Particles Interaction and Emerging Poromechanical Effects," *International Journal for Numerical and Analytical Methods in Geomechanics* 38, no. 1 (2014): 51–71.

46. L. Cheng, M. A. Shahin, and D. Mujah, "Influence of Key Environmental Conditions on Microbially Induced Cementation For Soil Stabilization," *Journal of Geotechnical and Geoenvironmental Engineering* 143, no. 1 (2016): 04016083.

47. M. Jiang, H. Yan, H. Zhu, and S. Utili, "Modeling Shear Behavior and Strain Localization In Cemented Sands by Two-Dimensional Distinct Element Method Analyses," *Computers and Geotechnics* 38, no. 1 (2011): 14–29.

48. J. Liu, A. Wautier, S. Bonelli, F. Nicot, and F. Darve, "Macroscopic Softening In Granular Materials From A Mesoscale Perspective," *International Journal of Solids and Structures* 193 (2020): 222–238.

Appendix A: 3D DEM Simulation Results

This appendix presents the simulation results of 3D DEM cemented samples with bridging type of cementation. The 3D DEM samples are subjected to drained triaxial compression test. The 3D DEM sample preparation, parameters of particles and triaxial compression simulation can be found in Zhang and Dieudonné [30]. The mechanical response is shown in Figure A1.

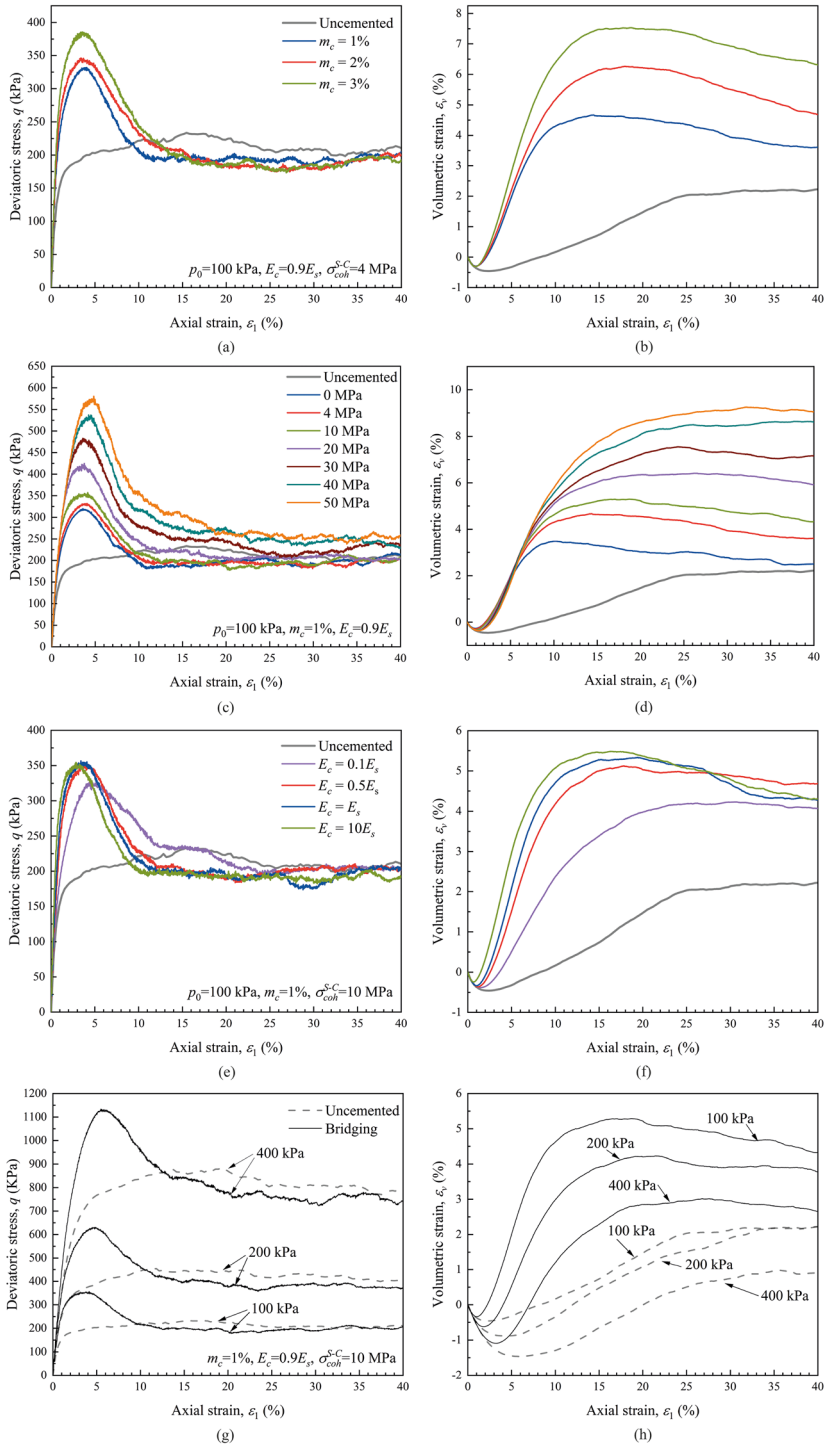

FIGURE A1 | Macroscopic mechanical response for 3D DEM samples with bridging type of cementation.